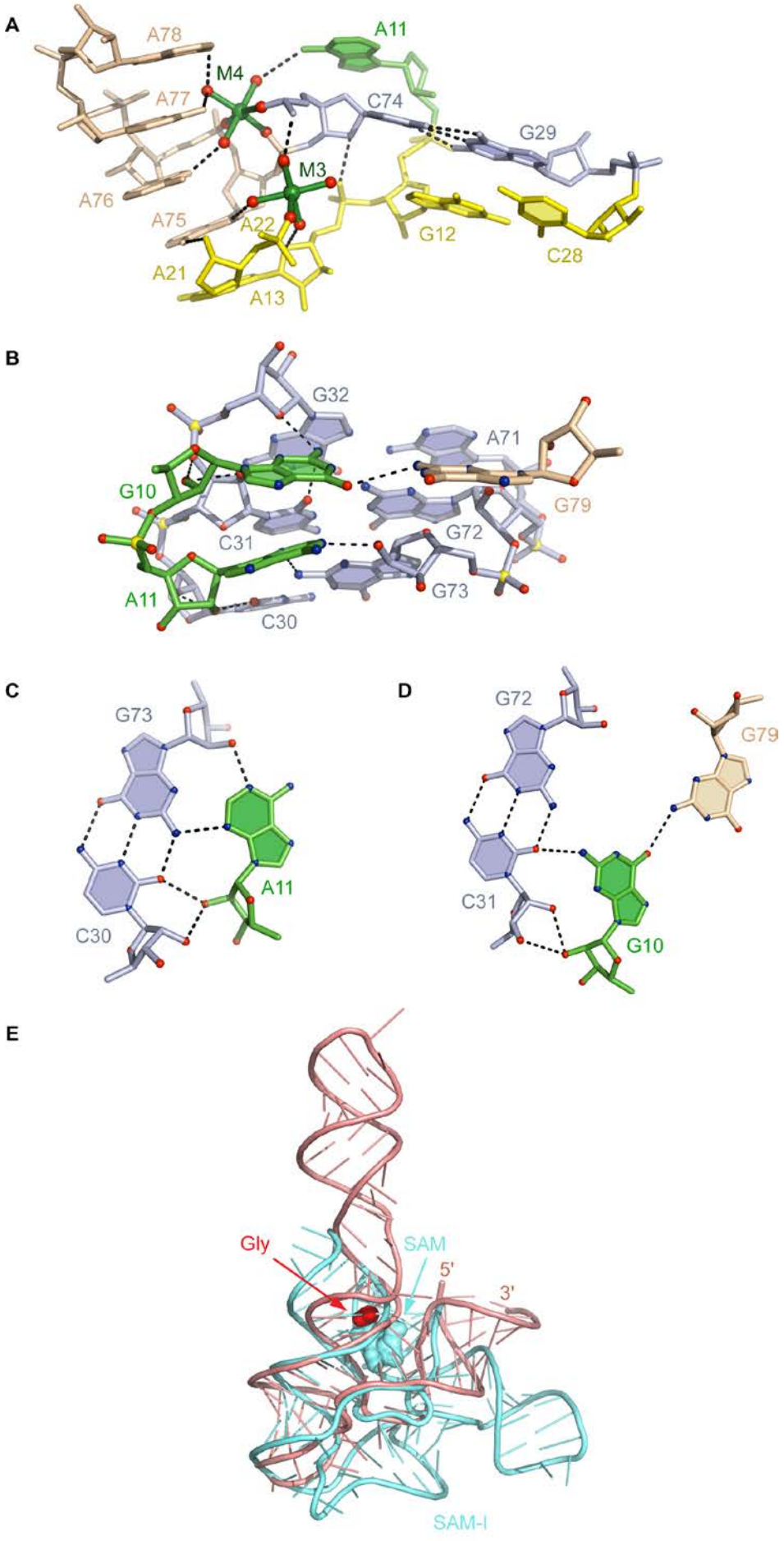
A
A78
A11
M4
A77
C74
G29
M3
A76
A75
A22
G12
C28
A21
A13
B
G32
A71
G10
G79
C31
G72
A11
G73
C30
C
G73
A11
C30
D
G72
G79
C31
G10
E
Gly
SAM
5'
3'
SAM-I

Figure S1. Tertiary Structure Elements in the Three-Way Junction of the Glycine Riboswitch and Comparison with Other RNA Structures, Related to Figure 1

(A) Formation of the turn between J3/1 and P2 by splayed apart C74 and A75. C74, positioned under the A11•(G73-C30) triple, makes a Watson-Crick pair with G29 and a hydrogen bond with phosphate of A13. A75 stacks on the base of A13 and makes a hydrogen bond with sugar of A21. Dashed lines depict putative hydrogen bonds formed by C74, A75 and water molecules coordinated by magnesium atoms M3 and M4. Mg^{2+} cations with coordinated water molecules are shown as green and red spheres connected by green sticks. Since the resolution of the structure does not allow clear separation of the electron density of Mg^{2+} cation and its coordinated water molecules, waters were positioned on the basis of direct Mg^{2+} coordination bonds. M3 coordinates directly to the non-bridging phosphate oxygens of A22 and A75, and uses outer-sphere interactions to contact C74, A75 and A13. M4 contacts directly non-bridging phosphate oxygens of A75, A76 and C74, and uses outer-sphere interactions to contact A11 and A76-A78. (B) Packing of the A11-G10 segment with the minor groove of P3. Dashed lines indicate putative hydrogen bonds from G10 and A11 to helix P3 and the joining region J3/1. (C) A11 forms type I A-minor motif with C30-G73 base pair. (D) G10 interacts with the sugar edge of C31 and Watson-Crick edge of G79. Since the base of G10 is twisted with respect to the plane of the C31-G72 base pair, G10 can make a hydrogen bond with ribose of G32 from the adjacent non-canonical G32•A71 base pair. Therefore, the A11-G10 segment is engaged in interactions with two consecutive base pairs of P3a and a nucleotide from J3/1. (E) Superposition of the glycine and SAM-I riboswitch (PDB ID: 2GIS) structures using nucleotides 58-60, 41-45 and 10-13 of the SAM-I riboswitch (molecule A), and 72-74, 28-32 and 9-12 of the glycine riboswitch (molecule A), respectively.

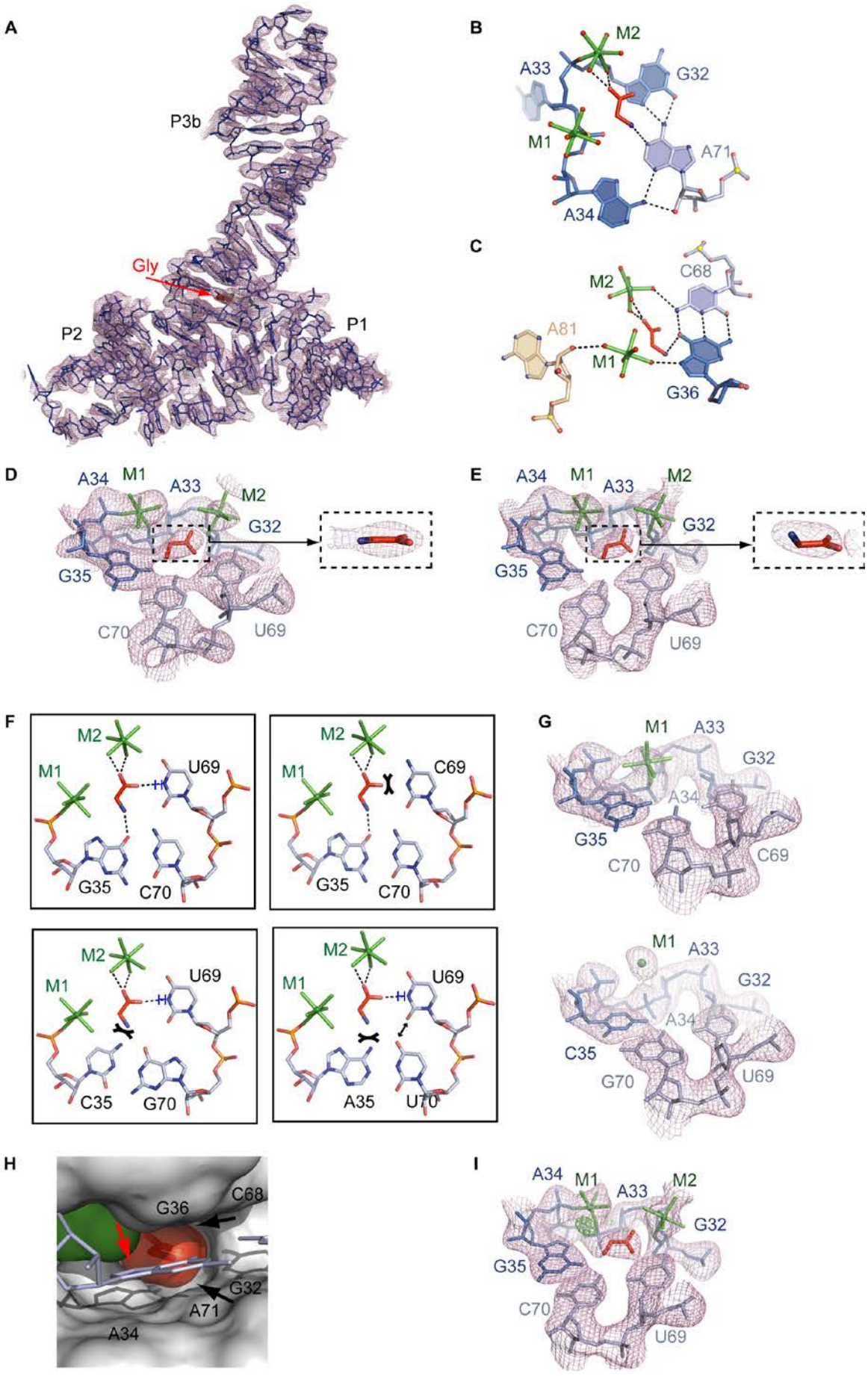
A
P3b
Gly
P2
P1
B
M2
A33
G32
M1
A71
A34
C
C68
M2
A81
M1
G36
D
A34
M1
A33
M2
G32
G35
C70
U69
E
A34
M1
A33
M2
G32
G35
C70
U69
F
M2
M1
U69
G35
C70
M2
M1
C69
G35
C70
M2
M1
U69
C35
G70
M2
M1
U69
A35
U70
G
M1
A33
G32
A34
G35
C70
C69
M1
A33
G32
A34
C35
G70
U69
H
G36
C68
G32
A71
A34
I
A34
M1
A33
M2
G32
G35
C70
U69

Figure S2. Detailed Views of the Glycine Binding Pocket, Related to Figure 2

(A) Experimental electron density map (contoured at 1 σ level) shown for molecule A of the refined riboswitch model. (B) The bottom layer of the glycine-binding pocket shown with Mg^{2+} cations and bound glycine in the molecule A of the native structure. Dashed lines indicate putative hydrogen bonds (<3.5 Å distance) formed between nucleotides of the A34•A71•G32 triple and between glycine and RNA. (C) The G36-C68 base pair constituting the roof of the glycine binding pocket. This view shows that the ammonium group of glycine is located within hydrogen bond distance from G36 and that M1 makes a water-mediated contact with A81. (D) and (E) Zoomed-in views of the portion of the experimental map (contoured at 1σ level) that corresponds to the bound glycine and adjacent nucleotides in the molecule A (D) and B (E) of the structure determined from the crystal of complex soaked in $[Ir(NH_3)_6]^{3+}$ cations. Insets show side views of the bound glycine. The structure refinements revealed that the ammonium group slightly rotates along the C-Cα carbon bond and can protrude out of the plane formed by other atoms of glycine because of the small open space around the group. Such conformational variability together with the moderate resolution of the structure possibly accounts for the lack of well-defined density map for the ammonium group. The map for the ammonium group becomes better after the B-factor sharpening procedure performed in Coot (data not shown). (F) Schematic of the glycine recognition in the non-modified riboswitch and schematics of the hydrogen bond disruptions in U69C, G35C/C70G and G35A/C70U mutants, based on the glycine-bound structure. Glycine and M2 are absent in the mutant riboswitch structures. Note that a hydrogen bond between nucleotide at position 69 and the water molecule coordinated to M2 may be preserved in the U69C mutant since the oxygen atom of the water molecule may use its one lone electron pair to form coordination bond with M2 and another one to form a hydrogen bond with a N4 proton of C69 (Shlyapnikov et al., 2001). Double arrow shows that the replacement of C70 by U places oxygen atoms of U69 and U70 close to each other (2.8 Å). The electrostatic repulsion between these oxygens may cause significant conformational adjustments in the pocket that prevent crystallization of this riboswitch mutant. (G) Glycine binding pocket in the U69C (top) and G35C/C70G (bottom) mutants shown with refined $2|F_o|-|F_c|$ maps (pink, 1σ level). Glycine and Mg^{2+} cation M2 are not observed in the structures. (H) Surface view inside the glycine-bound pocket showing the ammonium group of glycine (red) and Mg^{2+} cation M1 (green). Surfaces of G35 and C70 are omitted for clarity. Black arrows indicate small cavities around the ammonium group. Red arrow points at the Mg^{2+} coordinated water, which together with M1 participates in the formation of the pocket wall. Two Mg^{2+} cations were earlier found in metabolite binding pockets of thiamine pyrophosphate riboswitch (Edwards and Ferre-D'Amare, 2006; Serganov et al., 2006; Thore et al., 2008) and glmS riboswitch/ribozyme (Cochrane et al., 2007; Klein and Ferre-D'Amare, 2006). Unlike in the glycine riboswitch, in these riboswitches Mg^{2+} cations mediate interactions between RNA and negatively charged phosphates of the ligands. (I) Interpretation of the electron density map corresponding to Mg^{2+} cation M1. The moderate resolution of the structure does not allow clear visualization of the Mg^{2+} coordinated water molecules in the refined $2|F_o|-|F_c|$ maps (pink, 1σ level). However, omission of water molecules during refinement produced a strong positive $|F_o|-|F_c|$ map which disappeared after addition of coordinated waters. This view shows the $|F_o|-|F_c|$ map (green, 3σ level) calculated after the refinement of the M1 cation that lacks one of the coordinated waters.

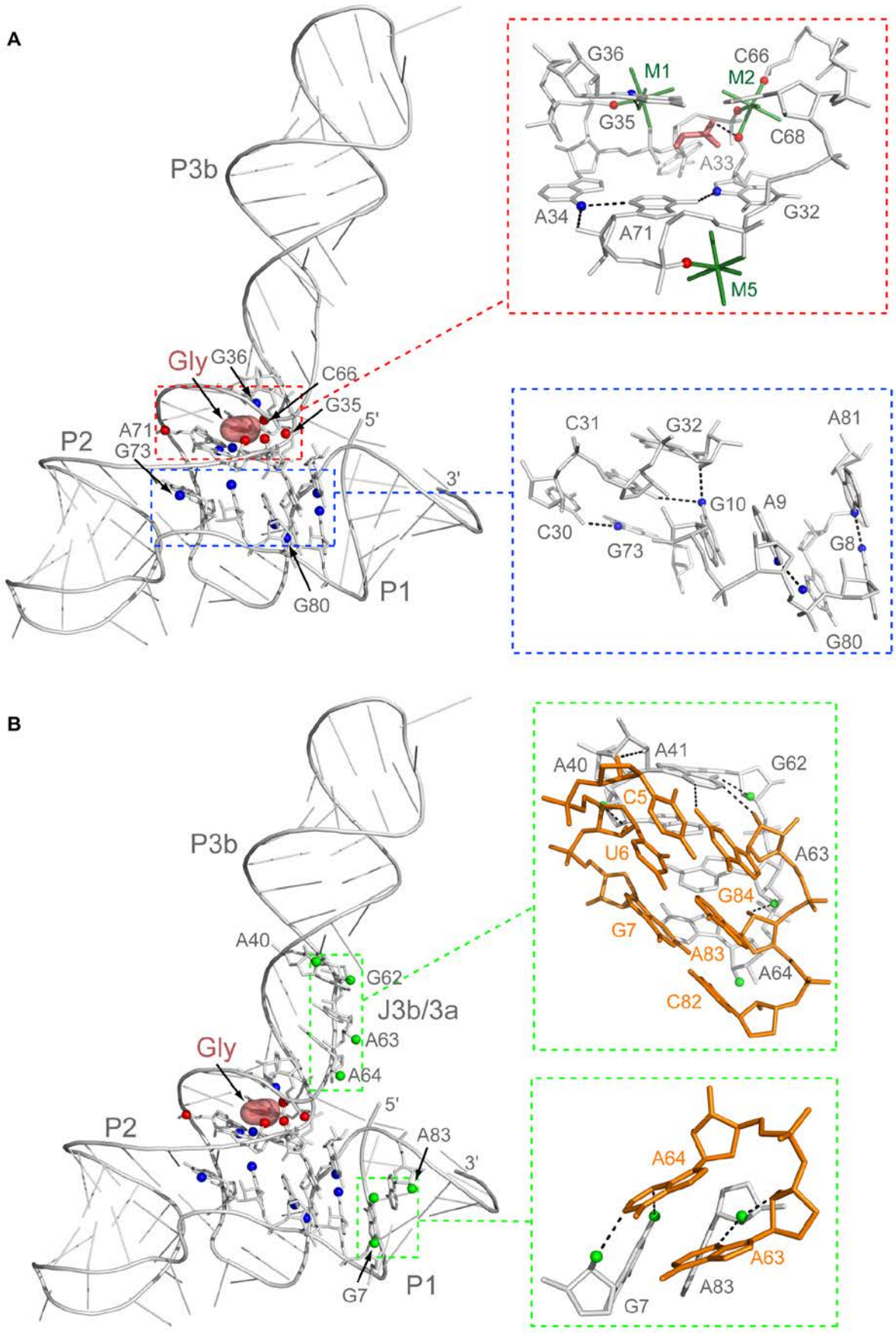
A
P3b
Gly
G36
C66
G35
A71
G73
P2
5'
3'
G80
P1
G36
M1
C66
M2
G35
C68
A33
A34
G32
A71
M5
C31
G32
A81
G10
A9
C30
G73
G8
G80
B
P3b
A40
G62
J3b/3a
A63
Gly
A64
5'
P2
A83
3'
G7
P1
A40
A41
G62
C5
U6
A63
G84
G7
A83
A64
C82
A64
A63
A83
G7

Figure S3. Projection of NAIM Sites on the Glycine Riboswitch Structure, Related to Figure 2

(A) The three-dimensional structure of the VCII riboswitch suggests that many functional group modifications in the domain II of *V. cholerae* tandem riboswitch (Kwon and Strobel, 2008) impair glycine binding by disrupting the three-dimensional structure of the riboswitch in the glycine binding pocket (top inset) and three-way junction (bottom inset). Dashed lines depict hydrogen bonds disrupted by nucleotide analog substitutions. Top inset: the replacement of G32 by deoxyribonucleotide eliminates the hydrogen bond with glycine carboxylate and the direct coordination bond with M2, thereby affecting glycine binding directly. The methylation of N6 of A34 or N7 of G32 prevents formation of the A34•A71•G32 triple essential for maintaining the binding pocket. The negative effects of other modifications are likely associated with coordination of Mg^{2+} cations. The methyl group at N7 of G36 would clash with M1, and the thio-modification of the G35 phosphate would interfere with direct coordination of M1. Similarly, glycine binding is abrogated with sulfur substitution of C66 and A33 phosphate oxygen atoms that directly coordinates to M2 and the phosphate oxygen of A71 that coordinates to M5. Bases of the middle layer are omitted for clarity. Bottom inset: each of four NAIM modifications located in the junctional core can disrupt the G8•A81 or A9•G80 non-canonical base pairs adjacent to A33. Two more modifications, methylations of the G10 or G73 bases, prevent placement of the J1/2 segment into the groove of P3 and, therefore, misalign two major parts of the junction. The G8C and G10C mutants prevent non-canonical pairing between J1/2 and J3/1 and disrupt formation of the junction and P1 helix. (B) The green spheres indicate the interference sites which do not disrupt the riboswitch domain structure and likely prevent the formation of cooperative interdomain interactions in the tandem riboswitch. Insets show the interference sites in the context of crystal packing interactions in the VCII RNA structure. The second riboswitch molecule of the asymmetric unit is in orange. Top inset: interference sites in the J3b/3a region. The deoxy-nucleotide substitutions of A40 and A63 eliminate hydrogen bonds in the A-minor triples, while the G62 substitution disrupts the pairing with A41 and may prevent productive A-minor interactions by misplacing A41. The 2'-hydroxyl of A64 does not participate in the crystal packing interactions and it is conceivable that it may form a hydrogen bond with the 2'-hydroxyl of C82 in the context of the natural riboswitch. In addition, this nucleotide may help restrict the position of the bulged out A65 and orient it for tertiary stacking interactions with the second riboswitch molecule. Bottom inset: modifications of G7 and A83 disrupt A-minor triples.

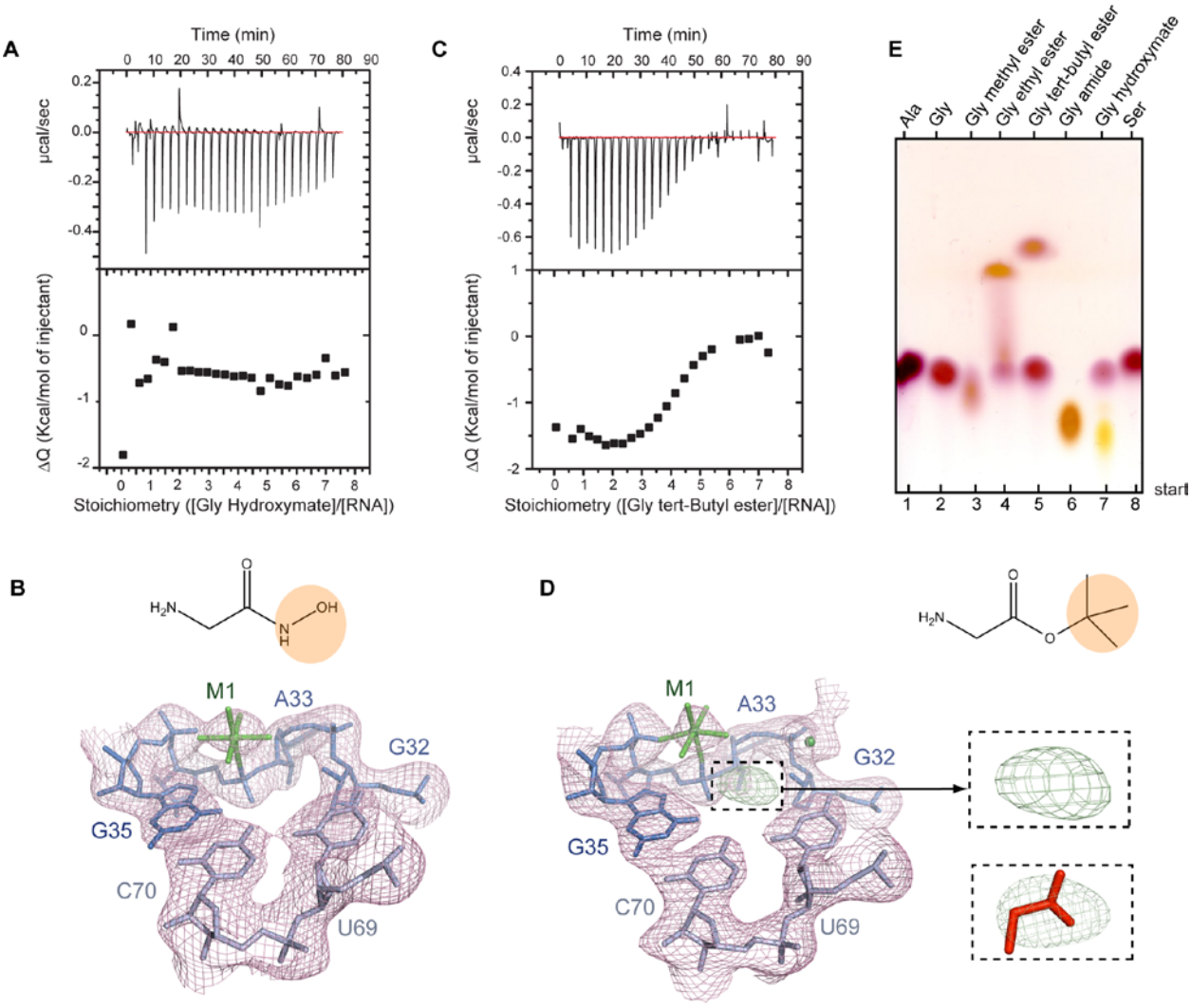

Figure S4. Binding of Glycine Analogs to the Glycine Riboswitch, Related to Figure 2
(A) Binding of glycine hydroxamate to VCII RNA measured by ITC. Raw measured heat changes as a function of time (top). Integrated heats of each injection (bottom). (B) The refined $2|F_o|-|F_c|$ electron density map (pink) contoured at 1σ level shows the absence of the bound ligand and M2 cation in the crystal grown in the presence of glycine hydroxamate. The structural formula of glycine hydroxamate is shown on top. Light-orange shading indicates chemical groups not present in glycine. (C) Binding of glycine *tert*-butyl ester to VCII RNA. Although the ligand shows binding to RNA, the dissociation constant and stoichiometry *n* value could not be reliably determined by data fitting. (D) The refined $2|F_o|-|F_c|$ (pink, 1σ level) and omit $|F_o|-|F_c|$ maps (green, 4σ level) calculated from the crystal grown in the presence of glycine *tert*-butyl ester do not show additional density for the t-butyl moiety. The omit map is zoomed-in in the inset. The omit $|F_o|-|F_c|$ map (4σ level) and glycine from the glycine-bound riboswitch structure are shown as a reference. The structural formula of glycine *tert*-butyl ester is shown on top. (E) Thin-layer chromatography of commercial glycine analogs (Sigma) run on silica gel plates (Sigma) in 30 % water and 70 % n-propanol and stained with ninhydrin. Hydroxamate, ethyl- and tert-butyl esters of glycine have two spots suggesting decomposition or impurities in the samples.

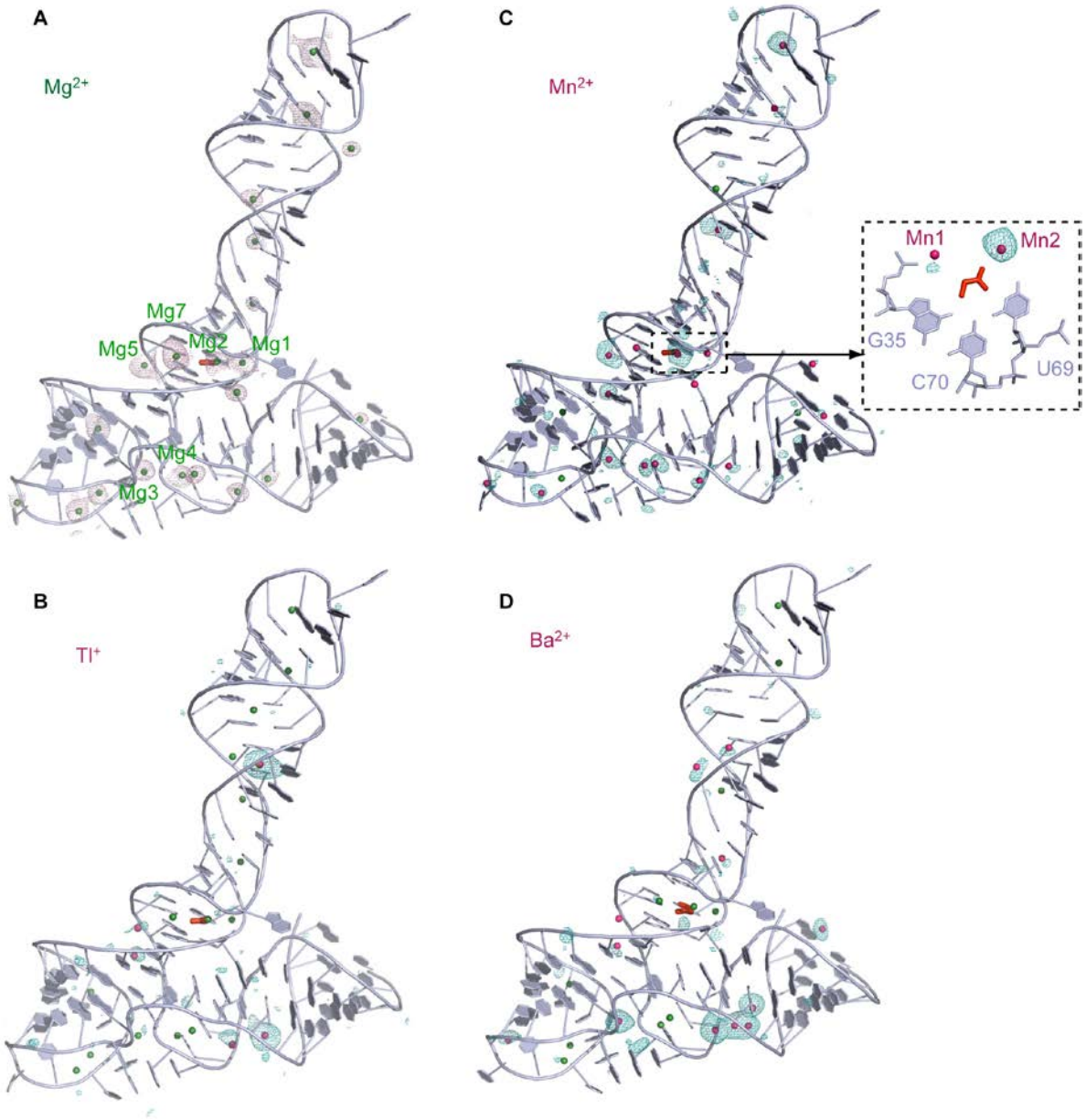

Figure S5. Metal Cations in the Riboswitch Structure, Related to Figure 3

(A) Native VCII RNA structure with Mg^{2+} cations as green spheres. The refined $2|F_o|-|F_c|$ electron density map (pink mesh) contoured at 1σ level is shows around cations. (B), (C) and (D) Riboswitch structures determined from the crystals soaked in 10 mM Tl-acetate for 8 h (B), 10 mM $MnCl_2$ for 4 h (C), and 10 mM $BaCl_2$ for 3.5 h (D) are shown with respective cation as magenta spheres. Anomalous maps (blue mesh) are contoured at 3σ level.

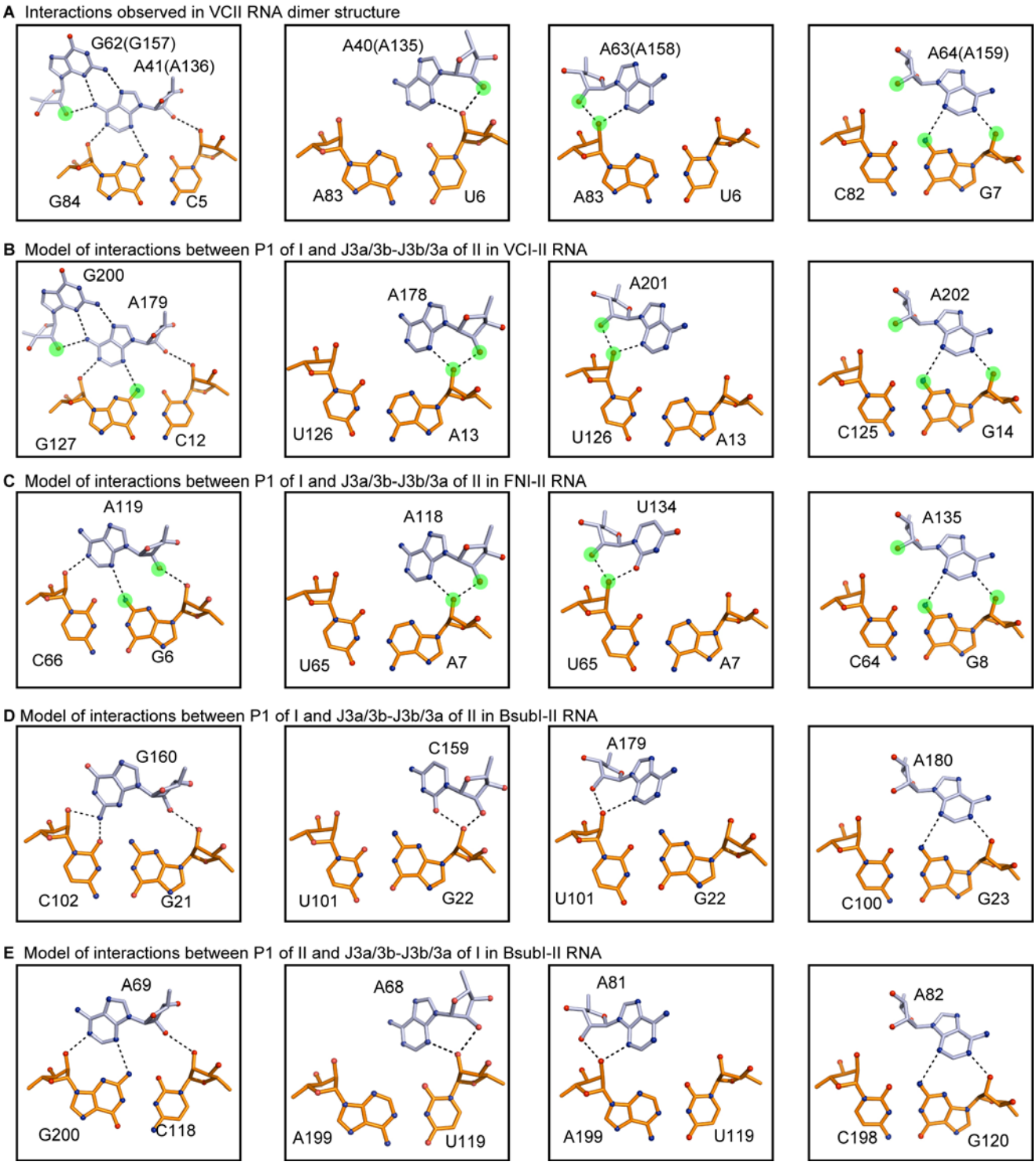

Figure S6. Modeling of Interdomain Interactions in Glycine Riboswitches, Related to Figure 4

(A) The A-minor crystal packing interactions in the VCII riboswitch RNA structure used as the basis for modeling of the interdomain interactions. Green spheres depict interference sites observed in the domain II of *V. cholerae* tandem riboswitch. The tandem VCII-II RNA is expected to form the same interactions in solution. The nucleotide numbering in parentheses corresponds to the VCII-II RNA. (B-E) Structure-guided models of interdomain interactions in the native tandem riboswitches from *V. cholerae* (B), *F. nucleatum* (C) and *B. subtilis* (D-E). Interference sites in panel C are from *F. nucleatum* riboswitch (Kwon and Strobel, 2008).

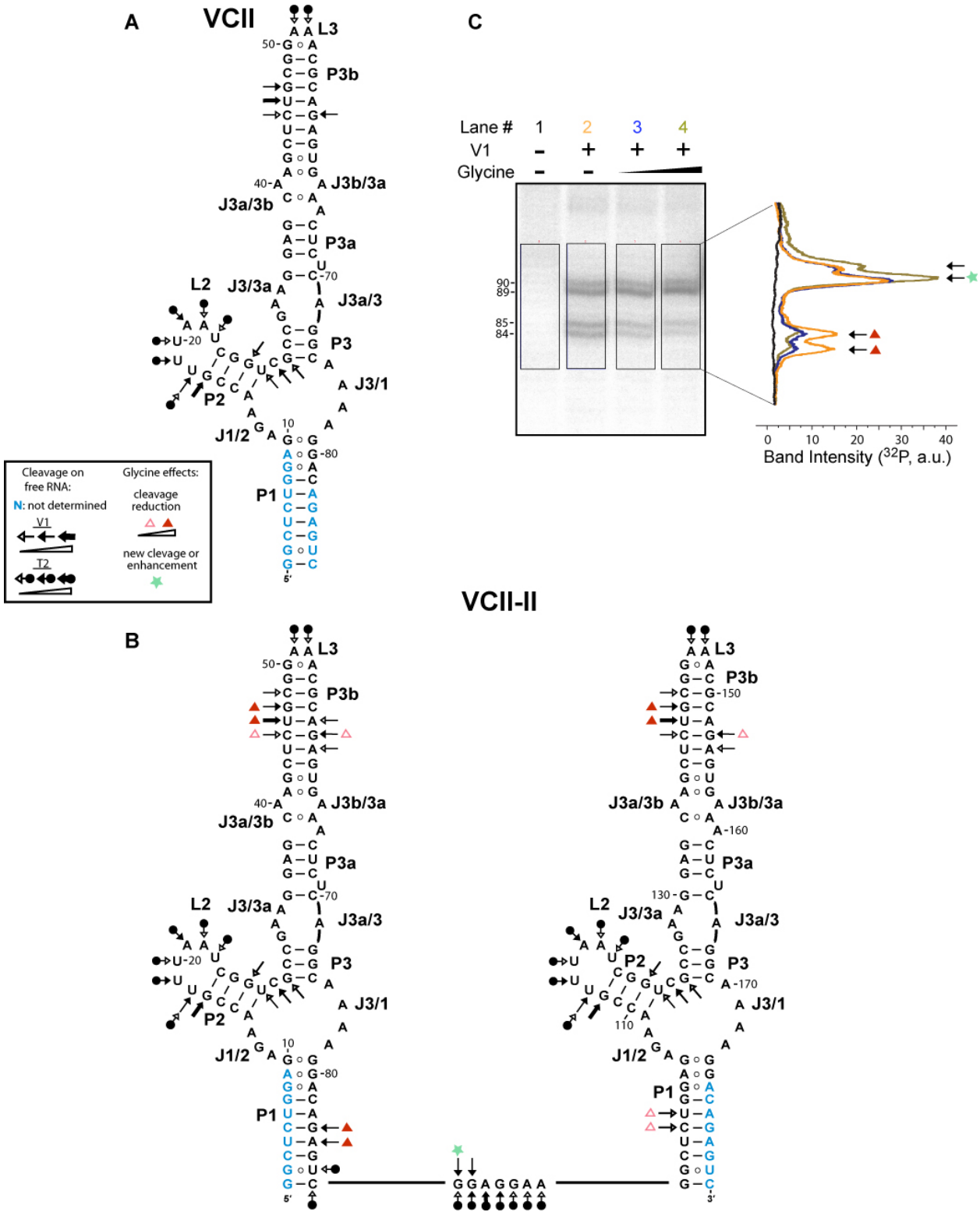
A
VCII
L3
P3b
J3b/3a
J3a/3b
P3a
L2
J3/3a
J3a/3
P3
P2
J3/1
J1/2
P1
Cleavage on free RNA:
N: not determined
V1
T2
Glycine effects:
cleavage reduction
new clevage or enhancement
C
Lane # 1 2 3 4
V1 - + + +
Glycine - -
90
89
85
84
0 10 20 30 40
Band Intensity (32P, a.u.)
B
VCII-II
GGAGGAA

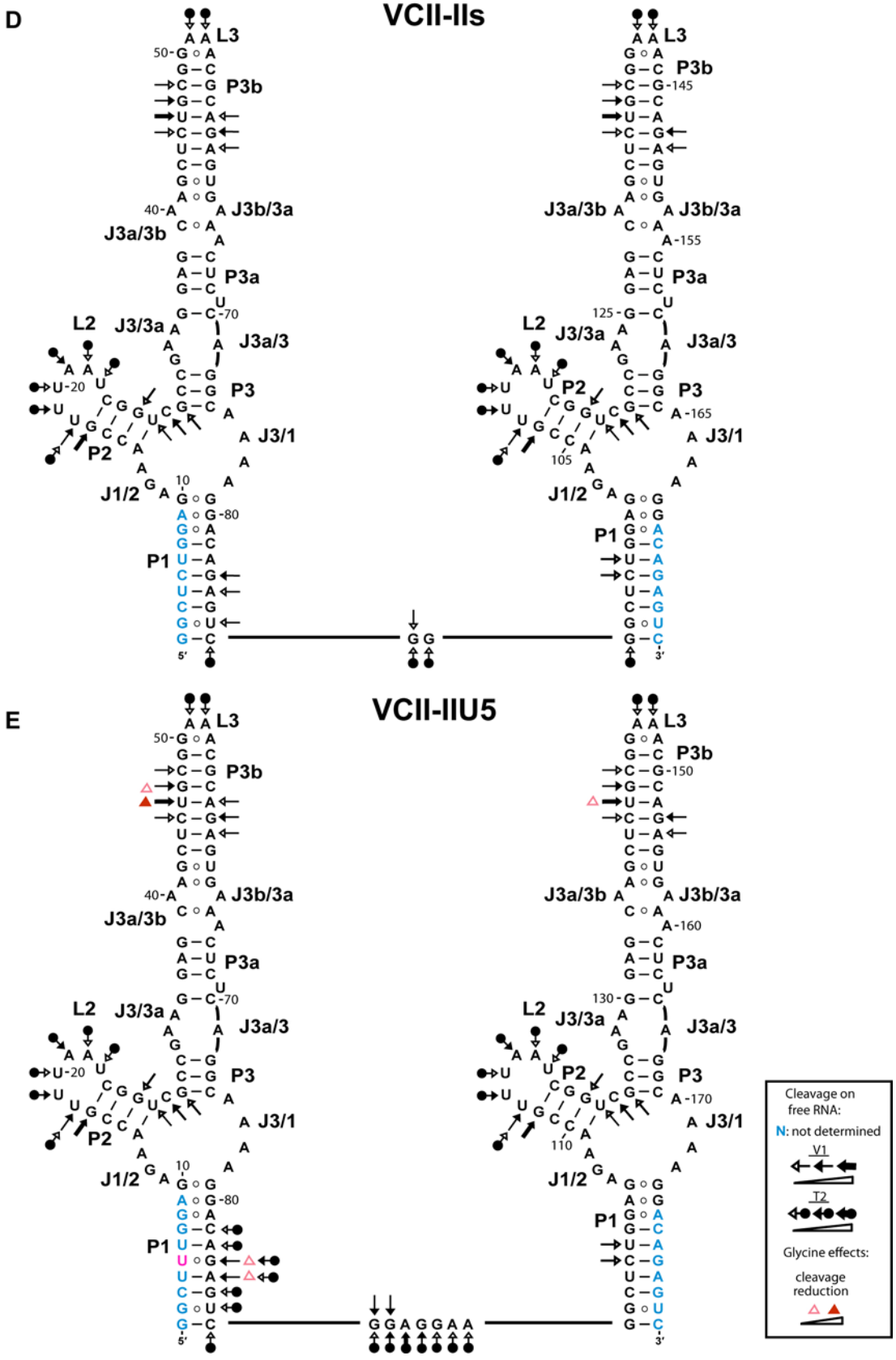
D
VCII-IIs
E
VCII-IIU5
L3
P3b
J3b/3a
J3a/3b
P3a
L2
J3/3a
J3a/3
P3
P2
J3/1
J1/2
P1
Cleavage on free RNA:
N: not determined
V1
T2
Glycine effects:
cleavage reduction

VCI

F

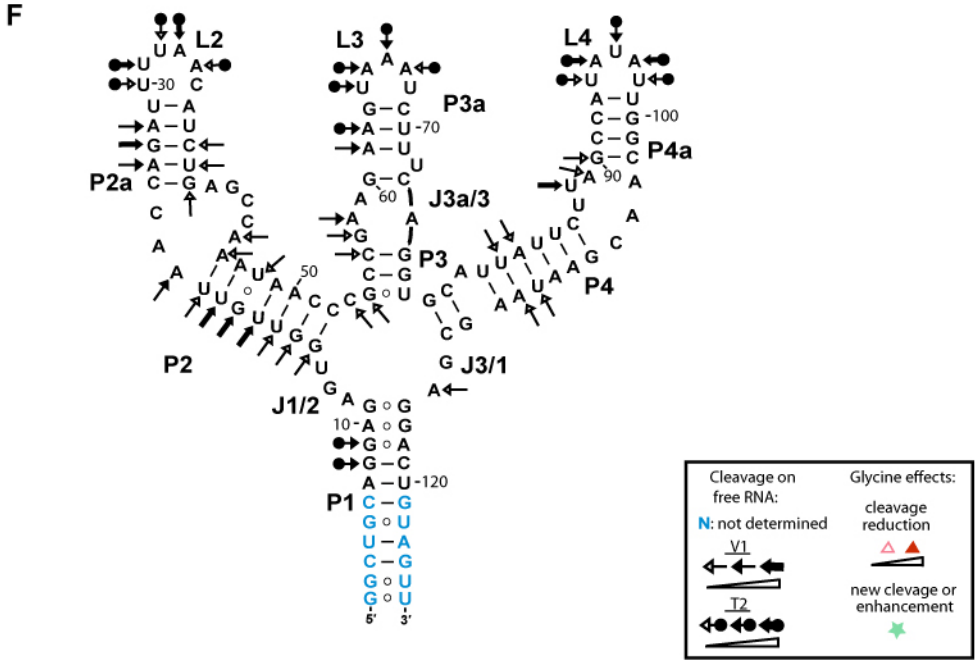
L2
L3
L4
P3a
P4a
P2a
J3a/3
P3
P4
P2
J3/1
J1/2
P1
Cleavage on free RNA:
N: not determined
V1
T2
Glycine effects:
cleavage reduction
new clevage or enhancement

VCI-II

G

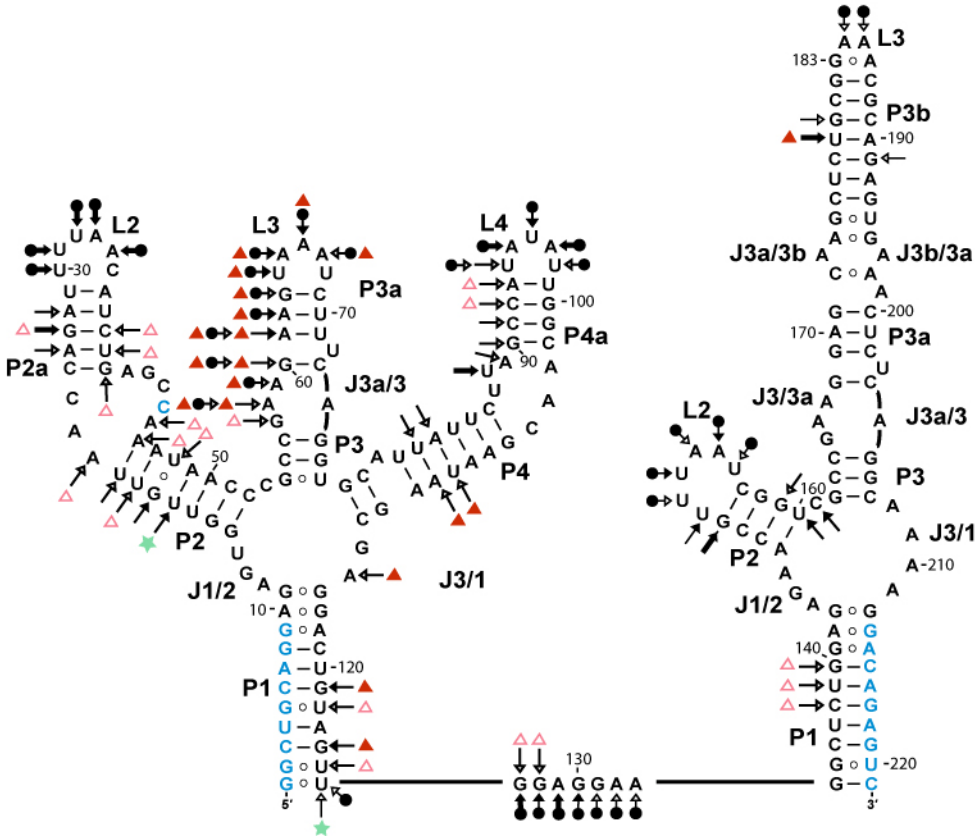
L2
L3
L4
P3a
P4a
P2a
J3a/3
P3
P4
P2
J3/1
J1/2
P1
J3a/3b
J3b/3a
P3b
J3/3a
L2
P3
J3/1
P2
J1/2
P1

Figure S7. Summary of the V1 and T2 Nuclease Footprinting Experiments Projected on the Secondary Structure Schematics, Related to Figure 5

(A) VCII riboswitch. (B) VCII-II riboswitch. (C) Visualization of an RNA region with reduced nuclease cleavage in the presence of glycine. This example shows the zoomed-in view of the P1 helix in the first domain of VCII-II RNA (left part of the panel). The profile analysis of the radioactivity in the rectangular area of each lane of the gel is shown on the right part of the panel. Profiles are color coded according to the lane numbers. Nuclease V1 cleavages, cleavage enhancements and protections are indicated on the right. (D) VCII-IIs mutant riboswitch. (E) VCII-II C5U mutant riboswitch. (F) VCI riboswitch. (G) VCI-II riboswitch. In addition to the similar protections in both VCI-II and VCII-II RNAs, VCI-II RNA displayed strong cleavage reductions in the J3a/3 region and P3a helix, and these also likely resulted from the interdomain interactions. In VCII-II RNA, these regions were not cleaved by nucleases, possibly because of the higher rigidity, and therefore protections could not be visualized. Unique protections observed along P2-P2a and P4-P4a helices suggest that VCI-II RNA forms a compact structure that prevents access of nucleases to these helices.

Extended Experimental Procedures

Alternative crystallization conditions

Crystals of glycine-bound riboswitch were also obtained using different protocols for complex preparation and crystal growth. The complexes of riboswitch and glycine were prepared by mixing 0.5 mM RNA with 2 mM glycine in a buffer containing 100 mM potassium acetate, pH 6.8, 1 mM spermine and 16 mM $MgCl_2$. Crystals were grown at 20 °C for a week using hanging-drop vapor diffusion method after mixing the complex at an equimolar ratio with the reservoir solution containing 0.05 M Mes-Na, pH7.1, 150 mM Mg-acetate, and 13-15 % MPD. For data collection, crystals were cryoprotected and flash frozen in liquid nitrogen as described in Experimental procedures.

Cell unit dimensions, space groups and crystal packing modes were found similar in both types of crystals obtained from either the 'MPD' or 'PEG8000' conditions.

Analysis of glycine analogs by thin layer chromatography (TLC)

The impurities of glycine analogs were detected by the TLC method. Glycine and its analogs used for crystallization were dissolved in water at 100 mM concentration. 0.5 µL of each sample was loaded on the Silica gel TLC plate (Sigma) and chromatography was carried out in a solvent system of water and n-propanol mixed at 30:70 (v/v) ratio. The TLC plates were dried and the loaded samples were visualized by spraying 2 % ninhydrin solution (Sigma, catalog # N7285). Several analogs showed more than one spot.

Interpretation of ITC experiments

Most ITC experiments were conducted at 20 and 40 mM Mg^{2+} concentration. These concentrations ensured sufficient signal upon glycine titration. At low Mg^{2+} concentrations, a signal-to-noise ratio was low, therefore, K_d values could not be determined with high accuracy.

The experimental ITC data of glycine titrated into single domain RNAs were integrated and analyzed using Origin 7.0 software (Microcal, Inc). The reference titration of the ITC buffer to RNA produced heats similar to those observed at the far end of the ligand-to-RNA titration. Therefore, the heat of sample dilution obtained at the ends of equilibrium titration was subtracted from the experimental titration data. The data, collected at Mg^{2+} cation concentration of 20 mM Mg^{2+} cation and over, showed excellent fitting to the 'single set of identical sites' model. The stoichiometry of glycine binding (floating parameter *n* in the fitting equation) ranged from ~0.93 to ~1.06. The binding experiments were conducted several times with independently prepared RNA samples and slightly different injection protocols. The binding constants and thermodynamic parameters from the independent experiments were averaged. The experiments conducted with 10 mM and 2 mM Mg^{2+} cations and the mutant A33U did not show strong response and therefore the binding affinity values are less accurate

ITC provides accurate thermodynamic measurements and, therefore, this method has been successfully used to study the cooperative binding of ligands to proteins (Brown, 2009) and assembly of macromolecular complexes (Recht and Williamson, 2004). However, ITC data may not be easily fitted to theoretical equations in systems with positive cooperativity (Tochtrop et al., 2002). The data analysis is especially challenging if binding sites on the macromolecule are cooperative and non-equivalent, as in the case of the natural tandem riboswitch from *V. cholerae*,

since one will not be able to determine the binding site heterogeneity and microscopic cooperativity without additional information on the occupancy of the binding sites (Di Cera, 2005). To analyze the data for the tandem riboswitches, we first estimated macromolecular binding constants and thermodynamic values using the 'single set of identical sites' model. This model provided better fits than the other two models ('two sets of binding sites' and 'sequential binding sites') in Origin 7.0, although initial points for some data sets had to be omitted. The *n* values were around 1.4 for the VCI-II RNA and in the range from 1.5 to 1.86 for the engineered tandem riboswitches, suggesting that glycine binds to more than one site. Since most values were much less than $n = 2.0$, expected for two independently bound glycine molecules, the RNAs either did not bind ligands stoichiometrically, or binding was cooperative. The single domain binding established that the minimum site occupancy was about 0.9, therefore the values much less than 1.8, most often observed in the non-altered tandem riboswitches, may indicate a cooperative response.

To further evaluate the data, we performed a global analysis of cooperativity using 'two-site heterogeneous association (A+B+B=ABB)' model in the SEDPHAT software package (Houtman et al., 2007). Raw ITC data were fitted using the following variables: inclA (fraction of RNA incompetent for binding), $\log(K_a1)$ (logarithm of the macroscopic constant for the first binding), ΔHAB (enthalpy change for the first binding), $\log_{10}(K_a2/K_a1)$ (cooperativity factor), and ΔH(AB)B-ΔHAB (enthalpy difference between the second and first binding). The analysis of the natural riboswitch data revealed a positive cooperativity with the cooperativity factor in the range from 1.4 to 1.8 (the value 1.0 corresponds to non-cooperative binding), closely matched the Hill coefficient value 1.6 determined earlier by the in-line probing experiments (Mandal et al., 2004). However, to get the best fitting, the fitting algorithm adjusted the inclA parameter to high values of 25-40%. The inclA parameter assumes that both binding sites behave identically. This may be not true in the case of the tandem RNAs, in which, despite cooperativity, the occupancy of each glycine binding site might be different and can not be assessed by an independent technique at this time. Although SEDPHAT fitting could accommodate more initial points than models from the Origin 7.0, the altered engineered tandem riboswitch data sets still required omission of data in the beginning of titration curves to get reasonable fitting curves. Therefore, we have chosen not to quantify and report cooperativity. It should be also noted that the K_ds and ΔHs values calculated using SEDPHAT and Microcal models were generally in the same range and imprecision of the values due to the fitting difficulties does not detriment the qualitative cooperativity mechanism we propose.

Supplemental References

Brown, A. (2009). Analysis of cooperativity by isothermal titration calorimetry. Int J Mol Sci *10*, 3457-3477.

Cochrane, J.C., Lipchock, S.V., and Strobel, S.A. (2007). Structural investigation of the GlmS ribozyme bound to its catalytic cofactor. Chem Biol *14*, 97-105.

Di Cera, E. (2005). Thermodynamic theory of site-specific binding processes in biological macromolecules (Cambridge, Cambridge University Press).

Edwards, T.E., and Ferre-D'Amare, A.R. (2006). Crystal structures of the thi-box riboswitch bound to thiamine pyrophosphate analogs reveal adaptive RNA-small molecule recognition. Structure *14*, 1459-1468.

Houtman, J.C., Brown, P.H., Bowden, B., Yamaguchi, H., Appella, E., Samelson, L.E., and Schuck, P. (2007). Studying multisite binary and ternary protein interactions by global analysis of isothermal titration calorimetry data in SEDPHAT: application to adaptor protein complexes in cell signaling. Protein Sci *16*, 30-42.

Klein, D.J., and Ferre-D'Amare, A.R. (2006). Structural basis of glmS ribozyme activation by glucosamine-6-phosphate. Science *313*, 1752-1756.

Kwon, M., and Strobel, S.A. (2008). Chemical basis of glycine riboswitch cooperativity. RNA *14*, 25-34.

Mandal, M., Lee, M., Barrick, J.E., Weinberg, Z., Emilsson, G.M., Ruzzo, W.L., and Breaker, R.R. (2004). A glycine-dependent riboswitch that uses cooperative binding to control gene expression. Science *306*, 275-279.

Recht, M.I., and Williamson, J.R. (2004). RNA tertiary structure and cooperative assembly of a large ribonucleoprotein complex. J Mol Biol *344*, 395-407.

Serganov, A., Polonskaia, A., Phan, A.T., Breaker, R.R., and Patel, D.J. (2006). Structural basis for gene regulation by a thiamine pyrophosphate-sensing riboswitch. Nature *441*, 1167-1171.

Shlyapnikov, S. V., Lunin, V.V., Blagova, E.V., Pembrandt, M. Betzel, Ch., and Mikhailov, A.M. (2001). X-Ray analysis of the magnesium-containing endonuclease from *Serratia marcescens*. Russian Journal of Bioorganic Chemistry 27, 370-377.

Thore, S., Frick, C., and Ban, N. (2008). Structural basis of thiamine pyrophosphate analogues binding to the eukaryotic riboswitch. J Am Chem Soc *130*, 8116-8117.

Tochtrop, G.P., Richter, K., Tang, C., Toner, J.J., Covey, D.F., and Cistola, D.P. (2002). Energetics by NMR: site-specific binding in a positively cooperative system. Proc Natl Acad Sci U S A *99*, 1847-1852.